Co-sensitized efficient Dye-Sensitized Solar Cells with TiO$_2$ Hollow Sphere/Nanoparticle Double-Layer Film Electrodes by Bi$_2$S$_3$ Quantum Dots and N719

Junmei Sun[1], Haiyong Guo[2,#], Li Zhao[2,*], Shimin Wang[2], Jinghua Hu[2], Binghai Dong[2]

[1] College of Biological Industry, Chengdu University, Chengdu 610106, PR China
[2] Hubei Collaborative Innovation Center for Advanced Organic Chemical Materials, Key Laboratory for the Green Preparation and Application of Functional Materials, Ministry of Education, Hubei Key Laboratory of Polymer Materials, Faculty of Materials Science and Engineering, Hubei University, Wuhan 430062, PR China.
[*]E-mail: zhaoli7376@163.com
[#]This authors contributed equally to this work.

TiO$_2$ double layer films composed of TiO$_2$ hollow spheres as overlayer and TiO$_2$ nanoparticles as underlayer were prepared, and Bi$_2$S$_3$ quantum dots have been successfully synthesized by hydrothermal method. Then the TiO$_2$ double layer films co-sensitized by Bi$_2$S$_3$ QDs and N719 dye were used as photoanode in dye-sensitized solar cells. The photoelectric properties of the DSSCs, with and without Bi$_2$S$_3$ QDs adsorption were studied. The results shows that the η of TiO$_2$/Bi$_2$S$_3$ DSSCs is enhanced with the increasing of Bi$_2$S$_3$ QDs amount in TiO$_2$ film and reaches up to 7.50% when sensitization time of Bi$_2$S$_3$ QDs arrives at 10 min. The improvement of performance is ascribed to the higher light harvesting, and the reduction of electron recombination as well as the enhancement of electron transport with the introduction of Bi$_2$S$_3$ QDs.

Keywords: Titanium dioxide; Double-layer film; Co-sensitization; Photoelectrochemical property

1. INTRODUCTION

Dye-sensitized solar cells (DSSCs) based on nanocrystalline TiO$_2$ have exhibited solar energy-conversion efficiencies up to 14% and are among one of the most promising alternative to photovoltaic cells due to their low-cost production, environment friendly components, and relatively high-photoelectric conversion efficiency [1-3]. A typical DSSC composed of a dye loaded nanocrystalline TiO$_2$ layer fabricated in a transparent conducting glass (FTO) as the working electrode, an electrolyte solution with I$^-$/I$_3^-$ redox reagents, and platinum (Pt) as the counter electrode[4]. Under illumination,

the dye molecules are excited and initial charge separation occurs by injection of an electron from the dye into the conduction band of the TiO_2. This electron is then transported to the external load via the nano-structured TiO_2 and the front transparent conductive oxide glass [5]. The mesoscopic TiO_2 film is at the heart of DSSCs, playing a fundamental role for the DSSC performance in light harvesting, charge generation, and charge transport [6,7]. Optimization and treatment of TiO_2 are highly desired to improve performance of DSSCs through the photoelectrodes. Other than TiO_2 nanoparticles, TiO_2 nanorod [8,9], nanowire [10,11], nanotube [12,13], nanosheets [14] and core-shell [15] structures have been extensively explored in DSSCs with intension of improving the overall photovoltatic conversion efficiency [16]. Nevertheless, these of nanoparticle-based solar cells.are higher than their photovoltaic performances It is now well-accepted that a high-efficiency photoelectrode for DSSCs should possess large surface area, high-harvesting efficiency, rapid electron transport, low electron recombination, and good electronic contact between TiO_2 film and FTO glass [17,18]. TiO_2 simultaneously satisfy these requirements, the bilayer structure and multilayer structure films have been investigated and applied in DSSCs. Wang *et al.* reported that in order to enhance light-harvesting efficiency, a multilayer structure with small particles as underlayer and large particles as overlayer was proposed and a best efficiency of 10.2% was attained with the multilayer structure using an anti-reflection film on the cell surface [19]. Akilavasan, J. *et al.* in 2015 also reported that TiO_2 photoelectrodes, which were fabricated based on TiO_2 nanoparticle/nanotube double-layer films, can efficient enhanced electron transport and light scattering effect and finally obtained an enhanced conversion efficiency applied on DSSCs system [20]. Inspired from these experiment results, we have recently demonstrated a novel TiO_2 double-layer film photoanode of DSSCs consisting of TiO_2 hollow spheres (HS) as overlayer and single-crystalline TiO_2 nanorod arrays (RA) as underlayer. This new-typed TiO_2 HS/RA DL film could improve the efficiency significantly of DSSCs which is owed to its synergic effects, i.e. the relatively large surface area of TiO_2 HSs for effective dye adsorption, high light-harvesting capability of rutile phase TiO_2 RAs, and rapid interfacial electron transport in one-dimensional TiO_2 RAs [14].

TiO_2 responds only in the UV region because of its large band gap [21]. Aside from above innovative methods, a promising solution to this problem is to modify TiO_2 with narrow band gap semiconductor quantum dots (QDs), such as CdS [22, 23], CdSe [24, 25], PbS [26,27] and Bi_2S_3 [28, 29] as light harvesters to increase obviously the efficiency of solar cells [30]. Semiconductor QDs as inorganic sensitizer have several significant advantages in solar cell application. In general, the QD provide the ability to match the solar spectrum better because their absorption spectrum can be tuned by simply controlling their sizes [31]. Furthermore, semiconductor QDs can generate multiple electron-hole pairs per photon, which could achieve a high charge harvesting efficiency [32-35]. Whereas charge collection in quantum dot sensitized solar cells (QDSSCs) has prove to be significantly more difficult, probably due to charge trapping on QD surfaces and the availability of more recombination sites. Furthermore, photocorrosion and electrolyte corrosion are inevitably taken place in QDSSCs. Interestingly, some organic molecules coating the QDs are able to reduce the corrosions. Then, a unique method called co-sensitization of the TiO_2 film with organic dyes and inorganic semiconductor QDS is used in DSSCs to further improve the photoelectric conversion efficiency of DSSC. Meng, K. *et al* demonstrated the co-sensitization DSSC with CdS and PbS QDs and dye N719, which elevate the open circuit voltage and consequently increase the efficiency from

3.10% by N719-sensitized TiO$_2$, to 3.93% and 4.18%, by the co-sensitized TiO$_2$ [22]. Sykora *et al* investigated the photoinduced charge transfer between CdSe nanocrystal quantum dots and Ru-polypyridine complexes [36].

Building from these ideas, here we examine the combination of co-sensitization and TiO$_2$ double layer film photoeleode composed of TiO$_2$ hollow spheres as overlayer and TiO$_2$ nanoparticles as underlayer. The overlayer have high specific surface area to adsorb dye molecules effectively and good light-scattering capacity, and then the underlayer demonstrates a potential blocking layer between FTO and hollow spheres overlayer. The double-layer film cell showed improved electron transport rate and better electronic contact between TiO$_2$ film and FTO conducting glass, which might increase the efficiency of the cell. The selection of organic and inorganic sensitizer is of high importance. Herein, we used N719 as the organic dye since it has high molar extinction coefficient that absorbs strongly in the red edge of the visible spectrum. Bi$_2$S$_3$ QDs are chosen as an inorganic sensitizer because it has a direct band gap semiconductor with E_g=1.4 eV, close to the optimum for photoelectric conversion and is of high optical absorption coefficient [37, 38]. Its light absorption is complementary to that of N719 dye. Furthermore, the N719 dye sensitize the prepared QD-sensitized TiO$_2$ film by covering the surface of nanoparticles. Consequently, the QDs avoid corroding in electrolyte. Peter et al. reported that they have used self-assembled layers of Bi$_2$S$_3$ nanoparticles to sensitize nanocrystalline TiO$_2$, which replaced the ruthenium dye used in conventional dye-sensitized solar cells, which can increase the long wavelength component of the photocurrent response [39].

Such a TiO$_2$ double layer films co-sensitized with dye N719 and Bi$_2$S$_3$ QDs can form a particularly promising solar cell structure. Due to the presence of many nano-size hetero-interfaces between the semiconductor QDs and the TiO$_2$ nanoparticles, it provides significant support both for light absorption and charge separation, two key steps in solar-to-electric energy conversion. We have used colloidal QDs allowing a higher control of nanocrystal size and prevent both multilayer adsorption and the blockage of nanochannels. The precise control of the QDs sensitization process has been utilized to study the effect of the increasing amount of QDs sensitizer in the occurrence and transfer of photo-exited electrons and e holes. In this paper, we have discussed a detailed synthesis process, characterization, and photoelectrochemical properties of this photoelectrode. The comparison of the properties between pure dye sensitization and co-sensitization TiO$_2$ double layer film electrodes is also investigated. These electrodes result in a significant energy conversation efficiency of 7.5% under simulated AM 1.5 illuminations, clearly demonstrated that dye N719 and Bi$_2$S$_3$ QDs co-sensitized TiO$_2$ double layer films can be promising photovoltaic device. This work points at emphasizing the correlation of fundamental studies in the rational development of more efficient photoelectrochemical cells.

2. EXPERIMENTAL SECTION

2.1. Preparation of TiO$_2$ double-layer film electrode

In the present study, the photoanodes are constituted a double-layer TiO$_2$ films. The opaque layer, with enhanced light scatting, contains of 600-900 nm hollow TiO$_2$ spheres (according to our

previous paper [14]). The transparent layer is formed by 25 nm nanocrystalline TiO_2 (P25, Degussa). The photoelectrodes were prepared by the doctor-blade technique onto the FTO glass. The as-prepared films were gradually heated to 500 °C through a programmed sintering process to obtain good electrical contact between the nanoparticles. Such a double-layer structure approves of contact between the substrate and electrode, meanwhile it enhances the light scattering ability increasing the performance of the cells.

2.2. Preparation of co-sensitized TiO_2 double-layer film electrodes

The preparation of Bi_2S_3 quantum dots were synthesized using the hydrothermal method. In brief, 1.8 g $Bi(NO_3)_3 \cdot 5H_2O$ was added to 80 mL deionizer water, under vigorous stirring for 10 min. Then 2 g $Na_2S \cdot 9H_2O$ were added to the above solution, stirring for another 10 min. The mixed solution was transferred into a 100 mL teflon-lined stainless steel autoclave and heated at 120 °C for 2 h. The obtained black precipitate was collected and washed with deionized water and anhydrous alcohol three times, respectively. The Bi_2S_3 QDs were deposited on TiO_2 film electrodes by dipping the film electrodes into 0.1 M ethanol solution of Bi_2S_3 QDs at room temperature. The amount of QDs coated on film electrode was controlled by adjusting the dipping time. The subsequent drying was done in vacuum furnance at 60 °C for 6 h. The TiO_2/Bi_2S_3 composite films were designated TB-X, where X (0, 5, 10, and 15) is related to the sensitization time of Bi_2S_3 QDs.

Then, co-sensitizatioin was performed by immersing the dried QD-sensitized film electrode in 0.5 mM N719 ruthenium dye (Solaronix S.A., Lausanne, Switzerland) ethanol solution at room temperature for 24 h. The dye-adsorbed electrode was then flushed fully with ethanol and dried. Eventually, by placing a platinum-coated FTO conducting glass on the co-sensitized photoanode separated by scotch tape spacer all around, the solar cell was fabricated in a typical sandwich-type cell Then the fabricated cell was clipped together as an open cell. The active area of the cells was 0.16 cm^2. An electrolyte was made with 0.3 M LiI, 0.05 M I_2, 0.6 M 1-propyl-3-methylimidazolium iodide and 0.5 M *tert*-butylpyridine in dry acetonitrile. The electrolytes were immited into the open cell from the edge,then due to capillary forces a thin layer of electrolyte was attracted into the inter-electrode space, and the cell was tested instantly.

2.3. Characterization and measurements

The morphology observation was performed on a scanning electron microscopy (SEM, JSM-5610LV JEOL), transmission electron microscopy (TEM, JEM-100SX, JEOL) and selected area electron diffraction (SAED), high resolution transmission electron microscopy (HRTEM, JEM-2100F). The structures of the samples were investigated by X-ray diffractometer (XRD D/MAX-III, Akishima-shi) with Cu-Kα radiation from 10° to 80°. Nitrogen adsorption-desorption isotherms were obtained on an ASAP2020 (Micromeritics Instruments Corp., Norcross, GA, USA) nitrogen adsorption apparatus. All the samples were degassed at 180 °C prior to Brunauer-Emmett-Teller (BET) measurement. The BET specific surface area (S_{BET}) was determined by a multipoint BET method using

the adsorption data in the relative pressure P/P_0 range of 0.05-0.25. A desorption isotherm was used to determine the pore volume at $P/P_0 =0.995$ was used to determine the pore volume and average pore size. UV-visible absorption spectra of the as-prepared samples were obtained by a UV-visible spectrophotometer (UV-2550, Shimadzu).

The photocurrent-voltage (*J-V)* characteristic curves were measured using an IM6 electrochemical analyzer (Zahner Elektrik, Germany) under simulated solar light at 100 mW cm^{-2} (1 sun) intensity produced by a solar simulator (Newport 91160). The electrochemical impedance spectroscopy (EIS) was performed on an electrochemical workstation (IM6, Germany) under 100 mW cm^{-2} illumination. The frequency range was explored from 0.01 Hz to 100 kHz, and the applied bias voltage and ac amplitude were set at open-circuit voltage of the DSSCs and 10 mV, respectively. The incident monochromatic photoelectric conversion efficiency (IPCE) was measured using Newport's QE/IPCE Measurement Kit. The measurements were repeated three times for each sample, and the experimental error was found to be within *ca*. 5%.

3. RESULTS AND DISCUSSION

3.1. Morphology and Phase Structures

Figure 1 shows the top view and cross-sectional SEM images of the double layer film. As illustrated in Figure 1 (a), TiO$_2$ hollow sphere overlayer (21 μm in thickness) and P25 nanometer particles underlayer (10 μm in thickness) can be clearly recognized. There is a compact P25 nanometer particles layer between FTO substrate and hollow sphere layer, influencing the bonding strength between the FTO substrate and the hollow sphere layer clearly and obstructs the charge recombination between the FTO and the redox couple. Figure 1 (b) clearly demonstrates that the sizes of the prepared TiO$_2$ hollow spheres are in the range of 400-900 nm.
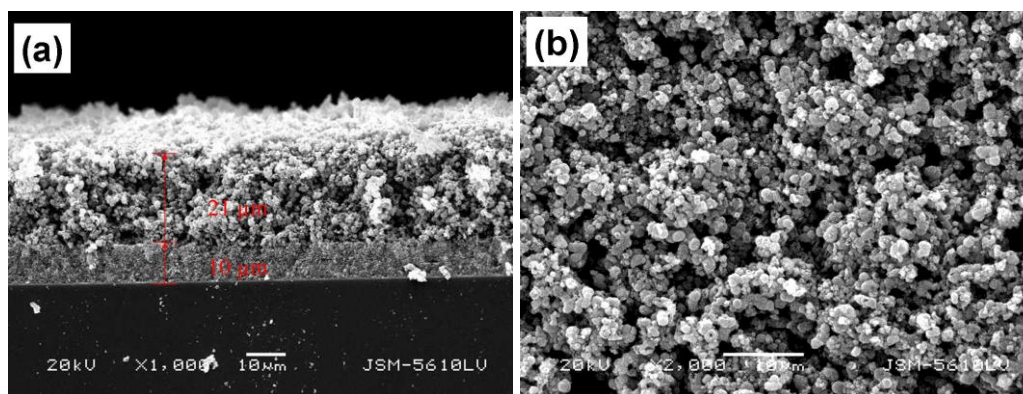
Figure 1 Top view and cross-sectional SEM images of double layer TiO$_2$ film electrode consisting of a P25 underlayer and a hollow spheres overlayer.
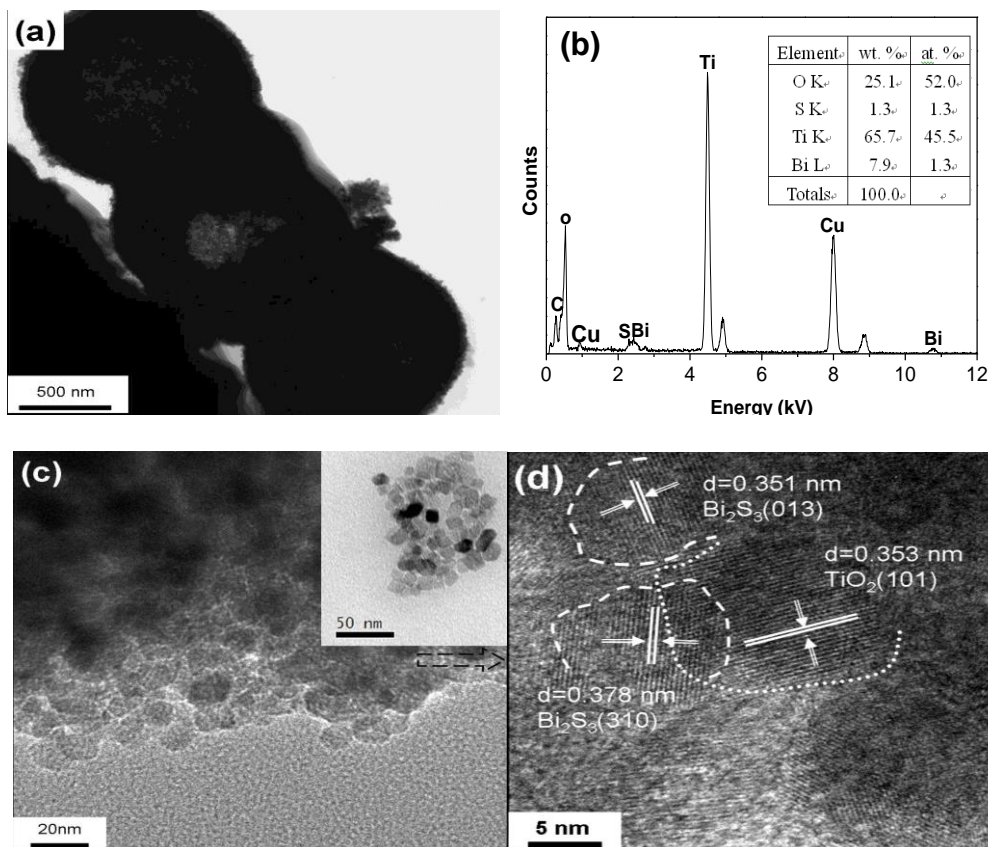
Figure 2 (a) TEM, (b) EDX pattern, (c) and (d) HRTEM images of Bi_2S_3 QDs-sensitized TiO_2 film electrode. The insets in Fig. 2 (c) show the synthesized pure Bi_2S_3 quantum dots.

To get more information about the TiO_2 hollow spheres, the sample was characterized by TEM. From Figure 2 (a) we can observe that the microspheres consist of about 500 nm hollow cavities and the shells of the hollow spheres are consist of a large number of TiO_2 nanocrystal particles. Due to these special structural features, the hollow spheres possess large surface area, efficient transport for electrolytes, and light scattering. The TEM image in Figure 2 (c) is a representative TiO_2 hollow spheres decorated with Bi_2S_3 QDs obtained for small portions of the QDs-sensitized films mechanically detached from the FTO substrates. After QDs sensitization for 10 min, some small discrete Bi_2S_3 QDs are visible as the dark spots on the surface of larger TiO_2 crystals. Inset in Figure 2(c) presents synthesized Bi_2S_3 sample, showing that dispersed Bi_2S_3 quantum dots have a uniform size distribution around 10 nm. Figure 2 (d) is a HRTEM image of the edge of a hollow spheres, the larger crystallite appearing in the right region of the image is identified to be TiO_2. The lattice spacing measured for these crystalline planes are about 0.353 nm, corresponding to the (101) plane of anatase TiO_2. The observed 0.351 nm and 0.378 nm fringes of the QDs on the TiO_2 crystals correspond to the (013) and (310) planes, respectively, of the rhombic phase of Bi_2S_3 (JPCD 17-0320). The composition of TiO_2/Bi_2S_3 composite films was measured by using energy dispersive X-ray spectroscopy (EDX) experiments, which were carried out in the TEM. Figure 2(b) shows typical EDX spectrum obtained from TiO_2/Bi_2S_3 composite films. In spectrum peaks associated with Ti, O, Bi and S elements are observed. Ti and O peaks result from TiO_2 hollow spheres, Bi and S are from sensitized Bi_2S_3 QDs

within hollow spheres, and the atomic ratio of O, S, Ti, and Bi is 52%, 1.3%, 45.5% and 1.3% , respectively. This provides powder evidence for the successful sensitization of Bi_2S_3 on the surface of TiO_2 films.

XRD was used to investigate the phase structure of the prepared samples. Figure 3 (a) presents XRD pattern of pure substrate and TiO_2/Bi_2S_3 samples. For the pure substrate sample, all the strong and sharp diffraction peaks are indexed to SnO_2 (space group: $P4_2$/mnm (136); a=4.750Å, c=3.198 Å, JCPDS No. 46-1088). For TiO_2/Bi_2S_3 sample, except the diffraction peaks of SnO_2 substrate, the anatase phase (JCPDS No. 21-1272, space group: $I4_1$/amd (141); a=3.785Å, c=9.514 Å) is dominant in the as-prepared double layer film electrode from P25 nanoparticles and hollow spheres. No characteristic diffraction peaks of Bi_2S_3 were observed. Two factors may be responsible for the absence of Bi_2S_3 peaks, one may be that only few QDs are attached to the TiO_2 film, the other may be that the QDs are highly dispersed on TiO_2 surface.
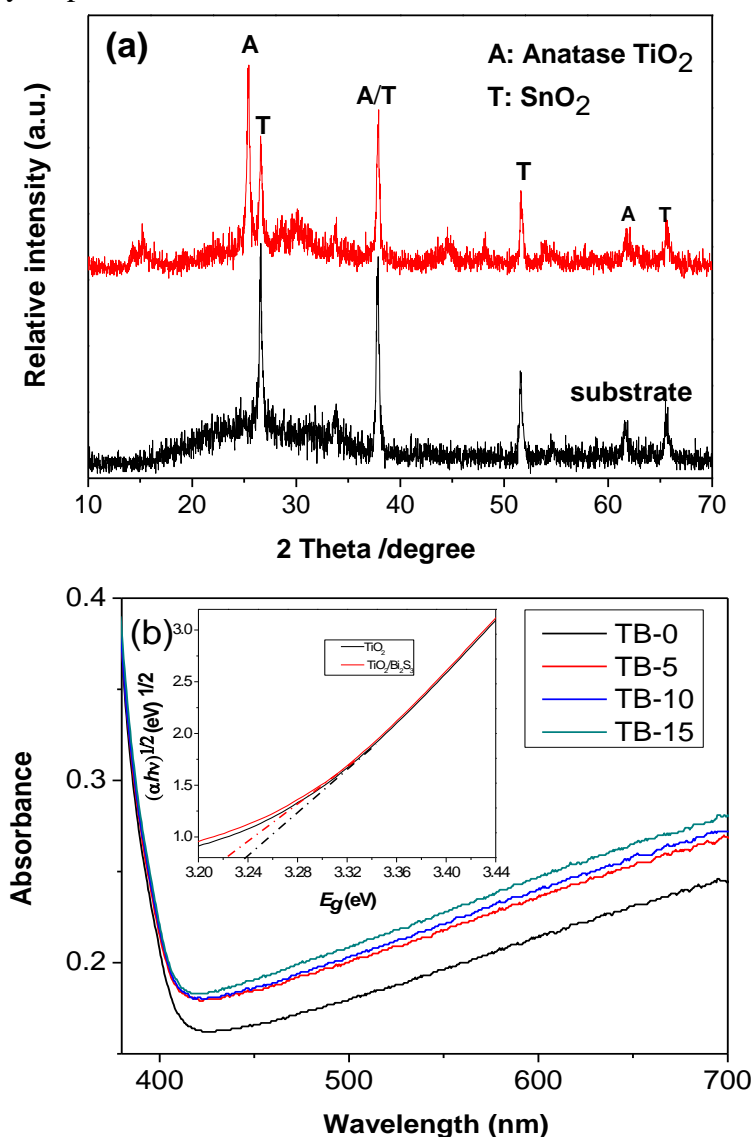
Figure 3. (a) XRD patterns, (b) UV-visible absorption spectra of TiO_2/Bi_2S_3 samples.

3.2. UV-vis Spectra Characterization

A comparison of the UV-vis absorption spectra of TiO_2/Bi_2S_3 samples is displayed in Figure 3(b). An obvious increase in the absorption at wavelengths less than 400 nm can be assigned to the intrinsic band gap absorption of anatase TiO_2 (3.2 eV). Interestingly, all the obtained TiO_2 double layer films also show a broad absorption around 400-700nm. Owing to multi-reflection of trapped incident light within the samples,both the hollow spheres itself and the voids between the hollow spheres are favorable for enhanced light absorption. The optical path length for light transport through the hollow spheres is longer with this method,which leads to a greater absorption capacity. The enhanced absorption capacity is advantageous for solar-electric conversation, thus will be further discussed below.

On the other hand, with increasing the time of QDs sensitization from 5 to 15 min, a small red-shift occurs in the absorption edgy. Such a red shift expands the light response range of TiO_2 film photoelectrode to the visible region and will increase the number of photogenerated electrons and holes able to participate in the photo-electric conversion. Moreover, there is an enhanced absorbance in the visible-light region (>400 nm) with increasing QDs content. A color change of the samples is also observed, when a low amount of black Bi_2S_3 QDs was introduced into pure TiO_2 film,they become darker, that is, from pale yellow to olive. On account of this increased absorbance, a more efficient utilization of the solar energy can be acquired. In consequence, it can be inferred that the introduction of Bi_2S_3 QDs in TiO_2 film is resultful for the visible-light response of the composite.

3.3. Specific Surface Areas and Pore Size Distributions

In Figure 4, it indicates the nitrogen adsorption-desorption isotherms and corresponding pore size distribution curve of pure TiO_2 and TB-10 composite samples. The nitrogen sorption isotherms for the aforementioned two samples are alike and display hysteresis loop at relative pressure (P/P_0) close to unity, which demonstrates the pressure of large mesopores and macropores, categorizing as type IV on the basis of BDDT classification (Figure 4). These isotherms exhibit H_2 hysteresis loops associated with the presence of ink-bottle-like pores with narrow necks and wider bodies. Both the samples indicate that bimodal mesopore size distributions, which are smaller mesopores with peak ore diameter of ca. 3.2 nm and bigger mesopores with peak pore diameter about 6.5 nm. This bimodal pore-size distribution is ascribed to two different pores: fine intra-aggregated pore within the agglomerated particles and large inter-aggregated pore produced by inter-aggregated secondary particles. The physicochemical properties of pure TiO_2 and TiO_2/Bi_2S_3 composite powders scraped from the film electrodes are shown in Table 1. Sensitization of Bi_2S_3 QDs on TiO_2 double layer film electrodes caused a little decrease in specific surface and pore volumes. On account of the specific surface area (m^2g^{-1}) and pore volume (cm^3g^{-1}) are presented by per gram of the samples,this is effortless to comprehend. The densities of Bi_2S_3 (7.7 gcm^{-3}) are larger than TiO_2 (4.8 gcm^{-3}), leading to the reduction of the BET surface area and pore volume. Since macroporous information of the film electrodes cannot be straightly obtained by N_2 adsorption-desorption analyses, the macroporous structures are clearly observed by the previous SEM and TEM images (Figure 1 and Figure 2),

indicating that the QDs-sensitized composite film contains 3-dimensional continuous macroporous mesoporous network from several, several tens, several hundred nm sized pores. The prepared hierarchically porous structures not only enhance the absorption of light, but also provide efficient transport pathways to electrolyte molecules.
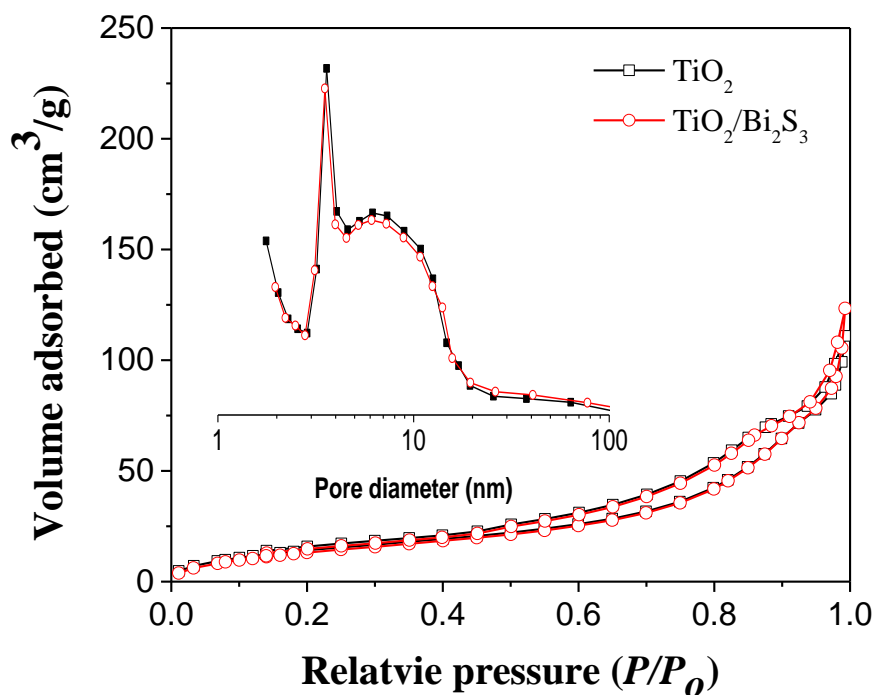
Figure 4 Nitrogen adsorption-desorption isotherms and the corresponding pore size distribution curves (inset) of the TiO_2 powders with and without QDs sensitization scraped from their 60 ^{o}C dried films.

Table 1. The physicochemical properties of TiO_2 and TiO_2/Bi_2S_3 composite powders scraped from the film electrodes.

Samples	S_{BET} (m^2g^{-1})	V_P (cm^3g^{-1})	APS (nm)	Porosity (%)
TiO_2	56.6	0.135	6.9	33.3%
TiO_2/Bi_2S_3	54.4	0.131	6.2	32.7%

3.4. Photoelectrochemical Property

Figure 5 displays the comparison of IPCE curves of the DSSCs made from the TB-0, TP-5, TP-10 and TP-15 film electrodes, in which IPCE were normalized to a common value of 1 at their maximum (530 nm). As observed, IPCE values increases sharply with increasing QDs sensitization time in the early times, demonstrating that more Bi_2S_3 QDs were absorbed into the electrodes and larger photocurrents occurred in the visible region. The photocurrents rooted in the processes of photoexcitation of electrons in the dye N719 and Bi_2S_3 QDs and their following transfer from dye

N719 and Bi_2S_3 QDs to TiO_2 electrodes. Thus, the IPCE value is found to somewhat decrease when the QDs sensitization time are increased to 15 min. This may result from Bi_2S_3 can absorb visible at the wavelengths above 400 nm, they display light-harvesting competition with the dye molecules and more, excess Bi_2S_3 nanoparticles can cat as potential barrier for charge transfer. As a result, that reduces the photovoltaic conversion performance for the co-sensitized TiO_2 solar cells. Furthermore, the small red-shift in the IPCE spectrum of TiO_2/Bi_2S_3 composite films with increasing QDs sensitization time as compared with the pure TiO_2 film should be due to the lower band gap of Bi_2S_3 QDs, which is consist with the results UV-vis absorption spectra.
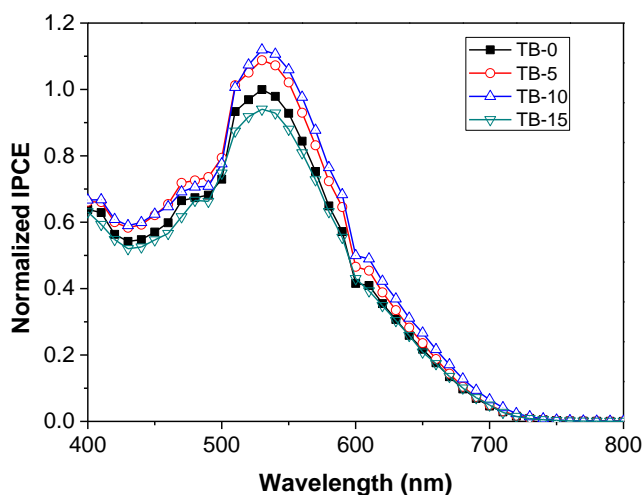
Figure 5. Normalized IPCE of DSSCs based the TB-0, TP-5, TP-10 and TP-15 TiO_2 film electrodes.
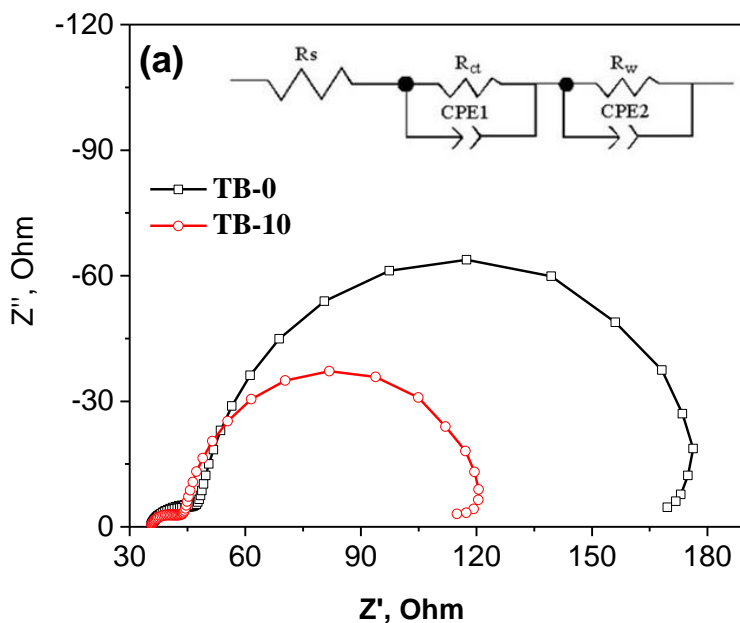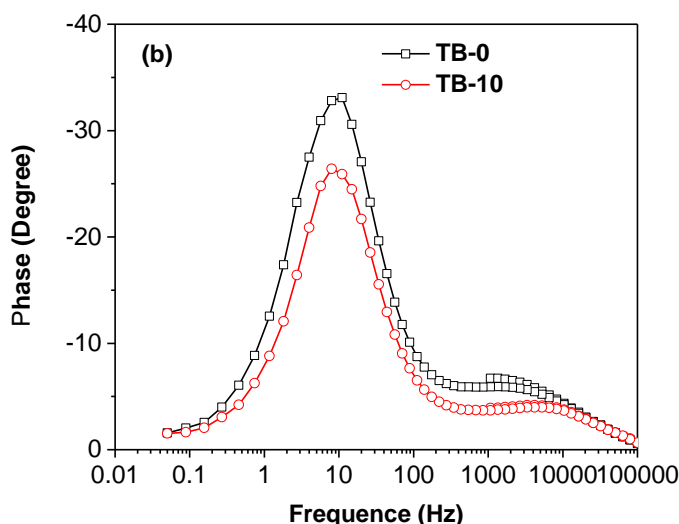
Figure 6. Nyquist plots (a) and Bode phase plots (b) of DSSCs based on the CT-0 and CT-10 TiO$_2$ film electrodes.

Electrochemical impedance spectroscopy (EIS) has been widely used to investigate electronic and ionic reaction in dye-sensitized solar cells (DSSCs). A theoretical model has been proposed to interpret the frequency response of the device.

The high-frequency response is on account of the charge transfer (or electrochemical reaction) at the Pt counter electrode, however the intermediate-frequency response is related to the electron transport and transfer at TiO$_2$/dye/electrode interface. The low-frequency region reflects Warburg diffusion process of I$^-$/I$_3^-$ in the electrolyte. However, in this experiment, only two semicircles could be observed (see Figure 6 (a)). The semicircle at low frequency region merged with the semicircle at the middle frequency region due to the weak resistance of ions transport in the electrolytes. From Figure 6 (a) we can see a large semicircle at low frequencies and a small semicircle at high frequencies, which were fitted with an equivalent circuit similar to the reported in the literature. The sheet resistance (R_s), charge transfer resistance (R_{ct}) and charge transport resistance (R_w) were obtained by fitting the impedance spectra of DSSCs using the equivalent circuit, as shown in Table 2. Apparently, compared with only the pure TiO$_2$ film, the values for R_{ct} and R_w of the TB-10 film have significantly decreased. This indicates a favored electron transport and the reduction of electron recombination when Bi$_2$S$_3$ QDs are introduced into TiO$_2$ double layer film.

Table 2. Parameters obtained by fitting the impedance spectra of DSSCs using the equivalent circuit in Fig. 6a

samples	R_s (Ω)	R_{ct} (Ω)	R_w (Ω)	τ_e (ms)
TB-0	35.0	18.3	136.6	14.4
TB-10	35.0	12.4	80.0	19.9

The Bode phase plots of EIS spectra are shown in Figure 6 (b). According to the EIS model developed [38, 39], the lifetime (τ_e) of injected electrons in TiO$_2$ film can be drawn by the position of the low frequency peak through the following equation: $\tau_e = 1/2\pi\, f_{max}$, where f_{max} is the maximum frequency of the low frequency peak. From it we can see that the cell based on the TB-10 film exhibits lower f_{max} of 8.01 Hz and higher τ_e of 19.9 ms as compared with the cell based on the pure TiO$_2$ film. Therefore, an appropriate amount of Bi$_2$S$_3$ QDs deposition on TiO$_2$ film has longer electron lifetime. From the analysis above, it is demonstrate that the introduction of Bi$_2$S$_3$ into TiO$_2$ film plays an important role in the performance change of DSSC. Figure 7 shows the schematic diagram of DSSC based on co-sensitized TiO$_2$ double layer film and the electronic diagram of FTO, TiO$_2$, Bi$_2$S$_3$, dye and electrolyte. Since the sensitization of the TiO$_2$ film by the QDs has been identified by IPCE, the conduction band edge E_c of certain Bi$_2$S$_3$ QDs must be above the E_c of TiO$_2$.
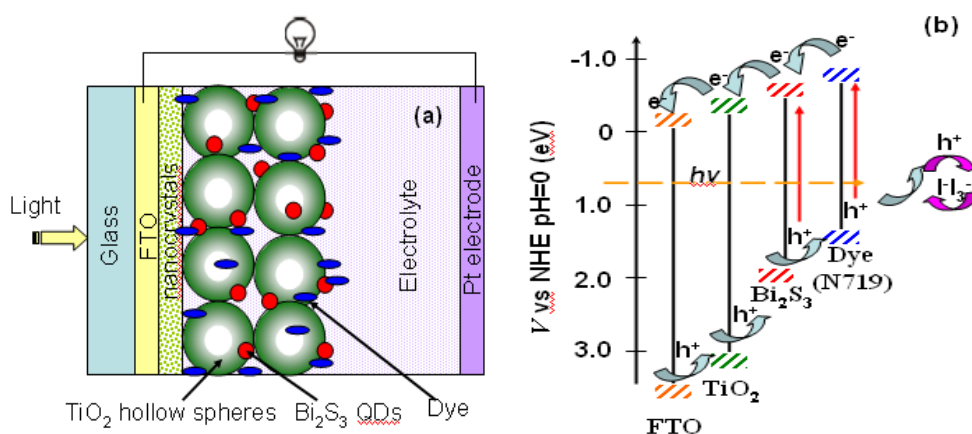
Figure 7. (a) Schematic diagram of DSSC based on co-sensitized TiO$_2$ double layer film electrode by Bi$_2$S QDs and N719, (b) electronic diagram of FTO, TiO$_2$, Bi$_2$S$_3$, dye and electrolyte.
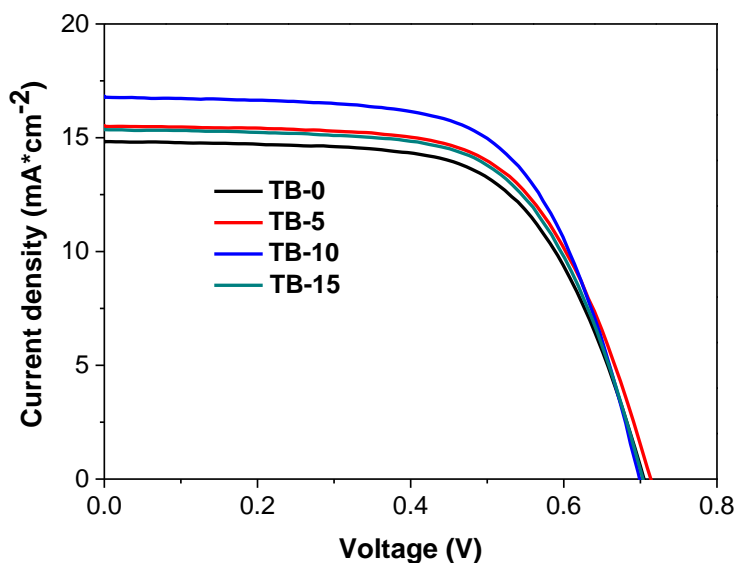
Figure 8. Comparison of the *J-V* characteristics of DSSCs made from TB-0, TB-5, TB-10 and TB-15 TiO$_2$ film.

This allows the electron injection from Bi_2S_3 QDs to TiO_2 and the holes immigration in TiO_2 excitons then to the valence band of CdS QDs. Figure 7(b) show stepwise energy levels of dye N719, Bi_2S_3 QDs, TiO_2 and FTO. Under light illumination, such energy levels are beneficial for electrons to transport from the excited state (LUMO) of dye N719 to FTO glass via QDs bridge. In addition, the holes transport to electrolyte via the different channel, which can prevent the charge recombination at the TiO_2/redox electrolyte interfaces and lead to the electrons diffusion and transport become easy. As described above, the DSSC based on the Bi_2S_3 QDs-sensitized TiO_2 film favor the electron transports through a longer distance (longer electron lifetime) with less diffusive hindrance to some extent (lower values for R_{ct} and R_w) and decreases the charge recombination and back-transport reaction. As a consequence, an appropriate amount of Bi_2S_3 QDs incorporated in TiO_2 enhance the cell performance of improving the electron transport and reducing the electron recombination.

Table 3. Comparison of the *J-V* characteristics of DSSCs based on TiO_2 and TiO_2/Bi_2S_3 composite films.

Samples	J_{sc} (mA.cm^{-2})	V_{oc} (V)	*FF*	η (%)
TB-0	14.82	0.703	0.637	6.64
TB-5	15.50	0.705	0.643	7.03
TB-10	16.77	0.698	0.641	7.50
TB-15	15.35	0.701	0.644	6.91

Comparison of the *J-V* characteristics of the DSSCs based on TiO_2 and TiO_2/Bi_2S_3 composite films electrodes is shown in Figure 8 and Table 3. The V_{oc} and *FF* vary little with QDs sensitization time. It is noteworthy that the photocurrent density (J_{sc}) and photoelectric conversion performances (η) of the DSSCs based on the TiO_2/Bi_2S_3 composite films electrodes are strongly dependent on the Bi_2S_3 QDs sensitization time. The value of J_{sc} increases from 6.64 to 7.50 with the increase in QDs sensitization time from 0 to 10 min. This is on account of that the incorporation of a small amount of Bi_2S_3 QDs into the TiO_2 films can reduce the charge recombination rate and resistance.As a consequence, it is normal to find that the values of J_{sc} η of a DSSC increase in the presence of a small amount Bi_2S_3 QDs. The enhanced J_{sc} is ascribed to the enhancement of the light harvesting and electron transport. Under optimal conditions, the η of the BT-10 solar cell is 7.50%. Obviously the enhancement of the photoelectrochemical properties is a contribution of the Bi_2S_3 QDs sensitizer. It can be supposed that the enhanced photoelectric conversion performance is on account of the following reasons. First of all, absorption spectrum was extended of into the visible region by TiO_2/Bi_2S_3 electrodes. In contrast with pure TiO_2 electrode, this electrode has intense absorption in the visible region, which raised the utilization rate of the solar energy substantially. Secondly, the Bi_2S_3 QDs have the merit of large QD extinction coefficients and generating multiple electron-hole pairs per photon. Thirdly, TiO_2 double layer film form a heterojunction with Bi_2S_3 QDs. This decreases the

charge transport resistance at the TiO_2/Bi_2S_3 QDs/dye/electrolyte interface, and decreased charge recombination of excited electrons and holes. However, at further higher QDs sensitization time, the conversion efficiencies decrease. This may be due to the following reasons: (1) before light arrives at the N719 dye layer through TiO_2 layer, Bi_2S_3 QDs can absorb some visible light and thus there exists a light harvesting competition between QDs and dye molecular with the increasing of Bi_2S_3 QDs amount; (2) the excessive Bi_2S_3 QDs can act as a kind of recombination center instead of providing an electron pathway; (3) pore size reduction (pore blockage) upon overloading of QDs sensitizer can give rise to poor electrolyte penetration. The reasons above result in the decrease of the total efficiencies.

4. CONCLUSIONS

TiO_2 double layer film co-sensitized by Bi_2S_3 QDs and N719 dye was used as photoanode in DSSCs to improve the photovoltaic performances. The results shows that the η of $TiO_2/$ Bi_2S_3 DSSCs is enhanced with the increasing of Bi_2S_3 QDs amount in TiO_2 film and reaches up to 7.50% when sensitization time of Bi_2S_3 QDs arrives at 10 min. The η improvement by maximum 13%, as compared with the one of the cell with pure TiO_2 electrode, should be ascribed to the increased Bi_2S_3 QDs sensitization, the higher light harvesting, and the reduction of electron recombination as well as the enhancement of electron transport with the introduction of Bi_2S_3 QDs. The results suggest that TiO_2 double film electrodes sensitized with Bi_2S_3 QDs and N719 dye will result in new features and desirable energy conversion performance.

References

1. J. M. Feng, J. J. Han, X. J. Zhao, *Prog. Org. Coat.,* 64 (2009) 268.
2. L. W. Chong, H. T. Chien, Y. L. Lee, *J. Power Sources*, 195 (2010) 5109.
3. T. Ganesh, R. S. Mane, G. Cai, J. H. Chang, S. H. Han, *J. Phys. Chem. C*, 113 (2009) 7666.
4. H. Kusama, H. Orita, H. Sugihara, *Sol. Energy Mater. Sol. C.*, 92 (2008) 84.
5. M. Hocevar, M. Berginc, M. Topic, U. O. Krasovec, *J. Sol-Gel Sci. Technol.*, 53 (2010) 647.
6. Q. Shen, T. Sato, M. Hashimoto, C. C. Chen, T. Toyoda, *Thin Solid Films*, 499 (2006) 299.
7. W. Lee, S. H. Kang, S. K. Min, Y. E. Sung, S. H. Han, *Electrochem. Commun.*, 10 (2008) 1579.
8. W. Y.Cheng, J. R. Deka, Y. C. Chiang, A. Rogeau, & S. Y. Lu, *Chem. Mater.*, 24 (2012) 3255.
9. W. Guo, C. Xu, X. Wang, S. Wang, C. Pan, C. Lin, & Z. L. Wang, *J. Am. Chem. Soc.*,134 (2012) 4437.
10. A. M. Bakhshayesh, M. R. Mohammadi, H. Dadar, & D. J. Fray, *Electrochim. Acta*, 90 (2013) 302.

11. L. Li, C. Xu, Y. Zhao, S. Chen, & Ziegler, K. J. *ACS appl. Mater. Inter.*, 7 (2015) 12824.
12. S. So, I. Hwang, & P Schmuki, *Energy & Environ. Sci.*, 8 (2015) 849.
13. K. Shankar, J. Bandara, M. Paulose, H. Wietasch, O. K. Varghese, G. K. Mor, T. J. Latempa, M. Thelakkat, C. A. Grimes, *Nano Lett.*, 8 (2008) 1654.
14. G. T. Dai, L. Zhao, J. Li, L. Wan, F. Hu, Z. X. Xu, B. H. Dong, H. B. Lu, S. M. Wang, J. G. Yu, *J. Colloid Interface Sci.*, 365 (2012) 46.
15. R. T. Ako, D. S. U. Peiris, P. Ekanayake, A. L. Tan, D. J. Young, Z. Zheng, & V. Chellappan, *Sol. Energy Mat. Sol. C.*,157 (2016) 18.
16. T. D. N. Phan, H. D. Pham, T. V. Cuong, E. J. Kim, *J. Cryst. Growth*, 312 (2009) 79.
17. S. Buhbut, S. Itzhakov, E. Tauber, M. Shalom, I. Hod, T. Geiger, Y. Garini, D. Oron, A. Zaban, *Acs Nano.*, 4 (2010) 1293.
18. J. Zhu, S. H. Wang, J. G. Wang, D. Q. Zhang, H. X. Li, *Appl. Catal. B*, 102 (2011) 120.
19. Z. S. Wang, H. Kawauchi, T. Kashima, H. Arakawa, *Coord. Chem. Rev.*, 248 (2004) 1381.
20. J. Akilavasan, M. Al-Jassim, & J. Bandara, *J. Nanophotonic.*, 9 (2015) 093091.
21. H. Chen, W. Y. Fu, H. B. Yang, P. Sun, Y. Y. Zhang, L. R. Wang, W. Y. Zhao, X. M. Zhou, H. Zhao, Q. Jing, X. F. Qi, Y. X. Li, *Electrochim. Acta*, 56 (2010) 919.
22. K. Meng, P. K. Surolia, O. Byrne, & K. R. Thampi, *J. Power Sources*, 275 (2015) 681..
23. H. K. Jun, M. A. Careem, & A. K. Arof, *Nanoscale res. Lett.*, 9 (2014) 69.
24. H. J. Yun, T. Paik, B. Diroll, M. E. Edley, J. B., & C. B. Murray, *ACS appl. Mater. inter.*, 8 (2016) 14692.
25. Y. B. Lu, L. Li, S. C. Su, Y. J. Chen, Y. L. Song, & S. J. Jiao, *RSC Adv.*, 7 (2017) 9795.
26. L.Tao, Y. Xiong, H. Liu, & W. Shen, *Nanoscale*, 6 (2014) 931.
27. M. A.Basit, M. A. Abbas, E. S. Jung, Y. M. Park, J. H. Bang, & T. J. Park, *Electrochim. Acta*, 211 (2016) 644.
28. I. Zumeta-Dubé, V. F. Ruiz-Ruiz, D. Díaz, S. Rodil-Posadas, & A. Zeinert, *J. Phys. Chem. C*, 118 (2014) 11495.
29. R. Schaller, V. I. Klimov, *Phys. Rev. Lett.*, 92 (2004) 186601.
30. J. Zhang, J. H. Bang, C. Tang, P. V. Kamat, *Acs Nano*, 4 (2010) 387.
31. P. Sudhagar, J. H. Jung, S. Park, R. Sathyamoorthy, H. Ahn, Y. S. Kang, *Electrochim. Acta*, 55 (2009) 113.
32. M. Hamada, S. Nakanishi, T. Itoh, M. Ishikawa, V. Biju, *Acs Nano*, 4 (2010) 4445.
33. H. Lee, M. K. Wang, P. Chen, D. R. Gamelin, S. M. Zakeeruddin, M. Gratzel, M. K. Nazeeruddin, *Nano Lett.*, 9 (2009) 4221.
34. J. J. H. Pijpers, R. Koole, W. H. Evers, A. J. Houtepen, S. Boehme, C. M. Donega, D. Vanmaekelbergh, M. Bonn, *J. Phys. Chem. C*, 114 (2010) 18866.
35. J. Chen, D. W. Zhao, J. L. Song, X. W. Sun, W. Q. Deng, X. W. Liu, W. Lei, *Electrochem. Commun.*, 11 (2009) 2265.
36. M. Sykora, M. A. Petruska, J. A. Aceuedo, I. Bezel, T. J. Meyer, V. I. Klimov, *J. Am. Chem. Soc.*, 128 (2006) 9984.
37. S. H. Im, Y. H. Lee, S. I. Seok, S. W. Kim, *Langmuir*, 26 (2010) 18576.
38. X. Q. Xu, S. Gimenez, M. S. Ivan, A. Abate, B. Juan, G. Xu, *Mater. Chem. Phys.*, 124 (2010) 709.
39. L. M. Peter, K. G. U. Wijayantha, D. J. Riley, J. P. Waggett, *J. Phys. Chem. B*, 107 (2003) 8378.